



Impact of Cosmic-Ray Feedback on Accretion and Chemistry in Circumstellar Disks

Stella S. R. Offner¹ , Brandt A. L. Gaches^{2,3} , and Jonathan R. Holdship⁴¹ Department of Astronomy, The University of Texas at Austin, 2500 Speedway, Austin, TX 78712, USA; soffner@astro.as.utexas.edu² Department of Astronomy, University of Massachusetts, 710 N Pleasant Street, Amherst, MA 01003, USA³ I. Physikalisches Institut, Universität zu Köln, Zùlpicher StraÙe 77, Köln, Germany⁴ Department of Physics and Astronomy, University College London, Gower Street, London WC1E 6BT, UK

Received 2019 May 24; revised 2019 August 20; accepted 2019 August 21; published 2019 September 26

Abstract

We use the gas-grain chemistry code UCLCHEM to explore the impact of cosmic-ray feedback on the chemistry of circumstellar disks. We model the attenuation and energy losses of the cosmic rays as they propagate outward from the star and also consider ionization due to stellar radiation and radionuclides. For accretion rates typical of young stars of $\dot{M}_* \sim 10^{-9}$ – $10^{-6} M_\odot \text{ yr}^{-1}$, we show that cosmic rays accelerated by the stellar accretion shock produce an ionization rate at the disk surface $\zeta \gtrsim 10^{-15} \text{ s}^{-1}$, at least an order of magnitude higher than the ionization rate associated with the Galactic cosmic-ray background. The incident cosmic-ray flux enhances the disk ionization at intermediate to high surface densities ($\Sigma > 10 \text{ g cm}^{-2}$), particularly within 10 au of the star. We find that the dominant ions are C^+ , S^+ , and Mg^+ in the disk surface layers, while the H_3^+ ion dominates at surface densities above 1.0 g cm^{-2} . We predict the radii and column densities at which the magnetorotational instability (MRI) is active in T Tauri disks and show that ionization by cosmic-ray feedback extends the MRI-active region toward the disk midplane. However, the MRI is only active at the midplane of a minimum-mass solar nebula disk if cosmic rays propagate diffusively ($\zeta \propto r^{-1}$) away from the star. The relationship between accretion, which accelerates cosmic rays, the dense accretion columns, which attenuate cosmic rays, and the MRI, which facilitates accretion, creates a cosmic-ray feedback loop that mediates accretion and may produce variable luminosity.

Unified Astronomy Thesaurus concepts: Cosmic rays (329); Astrochemistry (75); Protoplanetary disks (1300); Circumstellar disks (235); Magnetic fields (994)

1. Introduction

The local degree of gas ionization shapes many fundamental processes in star formation. It dictates which chemical reactions dominate, and consequently the abundances of various atoms and molecules (Wakelam et al. 2012). These in turn drive heating and cooling processes, which determine the gas temperature. Ionization influences gas dynamics by determining the strength of the coupling between the gas and the magnetic field, which sets the importance of non-ideal magnetic effects such as ambipolar diffusion (Fiedler & Mouschovias 1993). Ionization is especially critical to the properties and evolution of circumstellar disks (Dutrey et al. 2014). The level of ionization determines whether the magnetorotational instability (MRI) is active and thereby dictates the efficiency of angular momentum transport and accretion (Balbus & Hawley 1991; Gammie 1996). Regions with low ionization near the disk midplane, where the MRI is inactive, provide conditions favorable for planetesimal formation (Gressel et al. 2012). At late times, photoionization facilitates disk dispersal (Alexander et al. 2014).

Ionization in circumstellar disks is produced by a variety of processes. Far-ultraviolet (FUV) radiation, defined as photons with energies between ~ 6 and 13.6 eV , from the host star, other nearby stars, or the diffuse Galactic background ionizes the disk surface layers (Semenov et al. 2004; Perez-Becker & Chiang 2011). Stellar X-ray photons, predominantly produced by active stellar coronae, have a longer mean free path and ionize gas deeper within the disk (Semenov et al. 2004; Glassgold et al. 2007). Short- and long-lived radionuclides within the disk ionize through their decay products: $\sim 1 \text{ MeV}$ photons, positrons, electrons, and α -particles (Cleeves et al. 2013b; Padovani et al. 2018). Ionization due to radionuclides

only dominates near the midplane, however, where other sources are absent. High-energy protons and electrons, i.e., cosmic rays (CRs), which are able to reach gas with surface densities $> 100 \text{ g cm}^{-2}$, may also provide a substantial source of ionization (Umebayashi & Nakano 1981; Padovani et al. 2018). Although the Galactic CR background is significant ($\zeta \sim 10^{-16} \text{ s}^{-1}$, Indriolo & McCall 2012), most of these CRs are likely screened by the magnetosphere of the host star (Cleeves et al. 2013a). However, CRs coming from the star itself could provide significant ionization to the inner disk (Rodgers-Lee et al. 2017). Recent models suggest that the CR flux may be enhanced near accreting sources by CRs accelerated within jets or accretion shocks (Padovani et al. 2016; Gaches & Offner 2018).

Measuring the CR flux directly is challenging, since our Sun’s magnetosphere screens low-energy CRs. The best measurements of the interstellar CR background have been recorded by *Voyager I*; however, the shape of the spectrum of the Galactic CR background remains uncertain (e.g., Padovani et al. 2018). The CR ionization rate is consequently measured indirectly through ions, such as H_3^+ , which are produced through CR reactions with neutral gas (Indriolo et al. 2007, 2015). These measurements return the CR ionization rate for different pointings and suggest that the ionization rate due to the CR background is $\sim 10^{-16} \text{ s}^{-1}$ on average (Indriolo & McCall 2012). Observations toward protostellar sources, such as OMC-2 FIR4, suggest that the CR ionization rate may be higher near young sources (Ceccarelli et al. 2014; Favre et al. 2018). Astrochemical models can explain this ionization provided that CRs are accelerated locally by stellar accretion shocks (Gaches & Offner 2018; Gaches et al. 2019a). The measured and predicted ionization rates are sufficiently high to

suggest that such CRs will also affect the disk chemistry, properties, and evolution.

In this work we explore the impact of CRs accelerated by the accreting young host star on its circumstellar disk. We focus on slightly older, T Tauri-type sources, which host protoplanetary disks, have non-negligible accretion ($\dot{M}_* \gtrsim 10^{-9} M_\odot \text{ yr}^{-1}$), but are no longer embedded in a dense envelope. We consider the impact of different accretion rates, gas–magnetic field coupling, and assumptions about CR propagation. In Section 2 we describe our model setup and parameter choices. In Section 3 we present the resulting ionization rates, disk chemistry, and associated impact on the MRI-active regions. We discuss our results in Section 4, including the implications for observations and comparison to prior work. We summarize our conclusions in Section 5.

2. Study Parameters

2.1. Disk Initial Conditions and Chemistry

We adopt the time-dependent, gas-grain chemistry code UCLCHEM to compute the abundance distribution (Holdship et al. 2017). UCLCHEM treats each zone independently, taking as inputs the initial species abundance, local temperature, dust extinction to the surface, local FUV radiation field, CR ionization rate, and number density. We perform the calculations by separately modeling the vertical disk structure at each radius. Thus, we assume that radiation and CRs enter the disk from the surface, and we neglect contributions from radiation and CRs that may have propagated horizontally through the disk.

We define the disk density distribution in terms of the total column density, $N_{\text{tot}} = N_{\text{H}} + 2N_{\text{H}_2}$, where the surface density $\Sigma \equiv N_{\text{tot}} m_{\text{H}}$ and $m_{\text{H}} = 1.67 \times 10^{-24}$ g. The local number density of hydrogen is $n_{\text{tot}} \sim N_{\text{tot}}/h$. Given a flared disk, for a given column density, the radiation is incident at a grazing angle θ such that the effective column of extinction is $\sim N_{\text{tot}}/\theta$. Following Perez-Becker & Chiang (2011) we adopt $\theta = 0.3$. We assume that the inner disk is truncated at the magnetosonic radius (e.g., Manara et al. 2014; Hartmann et al. 2016):

$$r_m = \left(\frac{3B_*^2 R_*^6}{2\dot{M}_*(GM_*)^{0.5}} \right)^{2/7}, \quad (1)$$

where M_* is the star mass, \dot{M}_* is the accretion rate, R_* is the stellar radius, and B_* is the stellar magnetic field. For our fiducial model, $r_{\text{in}} = 0.021$ au. We adopt $r_{\text{out}} = 300$ au for the outer disk radius.

UCLCHEM does not solve the equations of thermal balance, so we assume that the disk is vertically isothermal and set the gas temperature according to (Glassgold et al. 2007; Perez-Becker & Chiang 2011)

$$T = 384 r_{\text{au}}^{-3/7} \text{ K}, \quad (2)$$

where r_{au} is the disk radius in au. This yields similar temperature values to (Offner et al. 2009)

$$T = \left(\frac{L_*}{4\pi\sigma r^2} \right)^{1/4} = 395 L_0^{1/4} r_{\text{au}}^{-1/2} \text{ K}, \quad (3)$$

assuming a star of $1 L_\odot$ where L_0 is the luminosity in L_\odot .

We adopt the chemical network from Quénard et al. (2018), which is constructed using the UMIST database plus additional reactions to hydrogenate C, N, and O atoms (McElroy et al. 2013;

Table 1
Elemental Abundances^a

Species	Reduced	Full
He	0.1	0.1
C ^{++a}	10^{-4}	10^{-4}
O ^a	10^{-4}	10^{-4}
S ^a	10^{-5}	10^{-5}
N ^a	0	6.1×10^{-5}
Mg ^a	0	3.8×10^{-5}
Si ^{++a}	0	10^{-7}

Note We compare two networks: (1) a simple network with only hydrogen, helium, carbon, oxygen, and sulfur reactions and (2) a network also including magnesium, nitrogen, and silicon reactions (Quénard et al. 2018).

^a Abundance relative to the total nuclear hydrogen density.

Wakelam et al. 2013). The network contains 522 species, including 211 on grain surfaces, and computes 3217 reactions altogether. We also consider a reduced network, in which only reactions with hydrogen, helium, carbon, oxygen, and sulfur are considered. Table 1 lists the elemental abundances for each network. We initialize the chemistry such that half of the hydrogen is molecular and half atomic, all of the carbon and silicon are ionized, and the remaining elements are neutral.

The formation and freeze-out of species on dust grains is a function of the dust number density and the number of binding sites on the grain surface (see Appendix A in Quénard et al. 2018). Here we assume a gas-to-dust mass ratio of 100, a dust grain mass density of $\rho = 3 \text{ g cm}^{-3}$, and a population with uniform grain size. Significant grain growth is expected in protoplanetary disks relative to the interstellar medium (ISM), especially near the disk midplane (e.g., Dullemond & Dominik 2004; D’Alessio et al. 2006). As the grain size increases, the total grain surface area declines as a_{gr}^{-1} (assuming a fixed gas-to-dust mass ratio). This reduces the area available to capture charged particles, which increases the gas ionization fraction, thereby influencing the diffusivity (Wardle 2007). Consequently, we expect that the details of the MRI are sensitive to the grain distribution. To quantify the effect of grain growth, we investigate three dust sizes. We adopt a grain radius of $a_{\text{gr}} = 1.0 \mu\text{m}$ for the fiducial value and compare this with small dust typical of the ISM ($a_{\text{gr}} = 0.1 \mu\text{m}$) and large dust representative of significant dust coagulation ($a_{\text{gr}} = 10 \mu\text{m}$). In practice, we expect the dust grain distribution to vary with scale height. However, a more sophisticated grain treatment than we apply here is required to capture this effect.

We make three modifications to UCLCHEM to include physical processes relevant for circumstellar disks. First, we modify the treatment of the CR ionization rate to permit variation as a function of position. This allows us to model the CR attenuation within the disk (see Section 2.4.1). The CR ionization rate is updated after each chemical solve, which also allows the CR flux to vary as a function of time.

Second, we include ionization due to X-rays. We compute the extinction of the X-ray radiation field using the column density to the disk surface, i.e., similar to the treatment of the FUV field (see Section 2.4.3). Last, we include ionization due to short-lived radionuclides. We treat this radionuclide ionization rate as a constant throughout the disk. Since radionuclides generally produce much lower ionization than other sources in our problem it acts as an ionization floor. We add the X-ray and radionuclide ionization rates to the CR

Table 2
Model Properties^a

Description	\dot{M}_* ($M_\odot \text{ yr}^{-1}$)	R_* (R_\odot)	r_A (au)	f_{acc}	ϵ	L_X (erg s ⁻¹)	a	a_{gr} (μm)
Fiducial model	10^{-7}	1.5	0.021	0.01	1.0	5×10^{29}	2	1.0
High accretion	10^{-6}	1.5	0.007	0.1	1.0	5×10^{29}	2	1.0
Low X-ray luminosity	10^{-7}	1.5	0.021	0.01	1.0	1×10^{29}	2	1.0
Partial coupling	10^{-7}	1.5	0.021	0.01	0.1	5×10^{29}	2	1.0
Low coupling	10^{-7}	1.5	0.021	0.01	0.01	5×10^{29}	2	1.0
Low accretion	10^{-9}	1.0	0.039	0.001	1.0	5×10^{29}	2	1.0
Small dust	10^{-7}	1.5	0.021	0.01	1.0	5×10^{29}	2	0.1
Large dust	10^{-7}	1.5	0.021	0.01	1.0	5×10^{29}	2	10.0
Diffusive attenuation	10^{-7}	1.5	0.021	0.01	1.0	5×10^{29}	1	1.0
Low accretion, diffusive attenuation	10^{-9}	1.0	0.039	0.001	1.0	5×10^{29}	1	1.0

Notes. Cosmic rays are accelerated assuming diffusive shock acceleration from the accretion shock at the stellar surface and attenuated as described above. See Gaches & Offner (2018) for details.

^a Accretion rate, stellar radius, Alfvén radius (disk inner radius), covering fraction of accretion, coupling between CRs and magnetic field between the star and disk, X-ray luminosity, attenuation exponent ($\text{CR} \propto r^{-a}$), and dust grain radius. All runs assume $L_{\text{FUV}} = 10^{30} \text{ erg s}^{-1}$ and a stellar field of $B = 1 \text{ kG}$.

ionization rate at each location to account for all secondary photons produced through X-ray and CR ionizations as well as non-thermal desorption reactions, whereby molecules are ejected from grain surfaces (Holdship et al. 2017). UCLCHEM also accounts for secondary electrons produced through CR interactions but assumes that they are thermalized, so they are not treated as new CR particles. We describe each source of ionization and the associated parameters in detail in Section 2.4.

2.2. Stellar Properties

We assume the host star has $1 M_\odot$ and explore several different accretion rates as summarized in Table 2. The sources represent T Tauri stars, which have approximately reached their final mass but continue to accrete via magnetospheric accretion from their disks at lower rates. T Tauri stars are observed to have magnetic fields of $\sim 1 \text{ kG}$, so we adopt that as our fiducial stellar field (Johns-Krull 2007).

We define the parameter f_{acc} , which represents the covering fraction of accretion hot spots on the stellar surface. The covering fraction appears to correlate with the accretion rate, i.e., stars experiencing lower rates of accretion have lower covering fractions (e.g., Hartmann et al. 2016). Here, we assume that the covering fraction is proportional to the accretion rate: $f_{\text{acc}} = 10^{-3} - 10^{-1}$ for accretion rates of $\dot{M}_* = 10^{-9} - 10^{-6} M_\odot \text{ yr}^{-1}$.

2.3. Shock Properties and Cosmic-Ray Acceleration

In order for diffusive shock acceleration to occur, the flow must have two properties. First, the gas must be supersonic, i.e., the shock velocity must exceed the thermal sound speed, $v_s > c_s$; second, the shock must be super-Alfvénic, $v_s > v_A$, where $v_A = B / \sqrt{4\pi\rho_i}$, B is the magnetic field, and ρ_i is the ion number density. The shock density can be written in terms of the accretion rate, \dot{M}_* , stellar radius, R_* , and accretion covering fraction:

$$\rho_i = \frac{\dot{M}_*}{f_{\text{acc}} 4\pi R_*^2 v_s m_H}, \quad (4)$$

where $\mu = 0.6$ for an ionized gas. We set the shock velocity as the freefall velocity at the stellar surface, $v_s = \sqrt{2GM_*/R_*}$. Combining these expressions, we can write the Alfvén criterion

in terms of the stellar parameters and accretion rate:

$$\begin{aligned} f_A &\equiv \frac{v_s}{v_A} \\ &= 3.7 \left(\frac{M_*}{1 M_\odot} \right)^{1/4} \left(\frac{\dot{M}_*}{10^{-7} M_\odot \text{ yr}^{-1}} \right)^{1/2} \left(\frac{B}{1 \text{ kG}} \right)^{-1} \\ &\quad \times \left(\frac{f_{\text{acc}}}{0.01} \right)^{-1/2} \left(\frac{R_*}{R_\odot} \right)^{-5/4}. \end{aligned} \quad (5)$$

This expression shows that the condition tends to be met for higher accretion rates and higher-mass stars, while “puffier” radii and lower accretion rates tend to reduce v_s , limiting the acceleration of cosmic rays.

For the initial CR spectrum, we adopt the calculation of Gaches & Offner (2018) for CRs accelerated through an accretion shock. This produces particles with energies up to a few GeV and has an energy dependence $\propto E^{-2}$. The particles lose energy through a variety of mechanisms as they propagate away from the source. We discuss our treatment of the attenuation of the CR spectrum and calculation of the CR ionization rate in Section 2.4.1.

2.4. Ionization Rates

Circumstellar disks have four primary sources of ionization: X-rays, cosmic rays, FUV radiation, and radionuclides. Each of these has a different relationship with radius and surface density and thus serves as the primary source of ionization in a particular part of the r - Σ parameter space. Figure 1 shows a schematic of the sources of ionization and the associated regions. Here we consider only local sources of ionization, namely those due to the central star, which generally dominate over external sources such as the Galactic X-ray, CR, and FUV backgrounds.

2.4.1. Cosmic Rays

CRs can penetrate column densities up to $\Sigma \sim 100 \text{ g cm}^{-2}$ before attenuating significantly, potentially allowing them to reach the disk midplane (Umebayashi & Nakano 1981). In practice, however, the influence of external CRs may be negligible due to shielding by the stellar magnetosphere or “T-Tauriosphere” (Cleeves et al. 2013a). In contrast, CRs from the source itself do not have this limitation

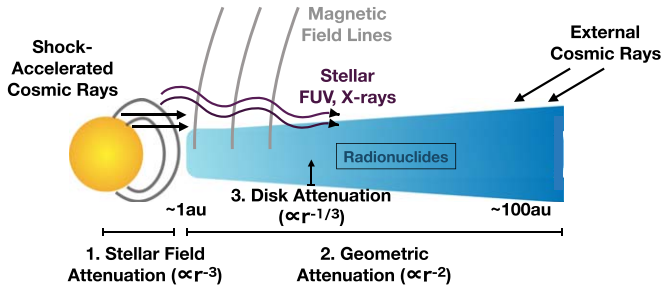


Figure 1. Schematic of our model.

(Rodgers-Lee et al. 2017). In particular, CRs accelerated at the stellar surface due to accretion shocks may provide a significant source of ionization (Padovani et al. 2009, 2018; Gaches & Offner 2018). Gaches & Offner (2018) showed that accreting protostars are a strong source of CRs, which impact the ionization of the dense core and larger molecular cloud. Here we explore the impact of CRs accelerated in accretion shocks on the chemistry and dynamics of circumstellar disks.

Like photons, CRs attenuate geometrically as they propagate outward from the central star and also suffer energy losses via interactions with gas along their path. Exactly how CRs propagate outward is not known, since it is a function of the magnetic field geometry, gas density, and degree of turbulence. Qualitatively, the flux of CRs declines as $\propto r^{-a}$, where the two limits are free-streaming ($a = 2$) and diffusive ($a = 1$). Gaches & Offner (2018) suggested that the high CR fluxes accelerated by the accretion shock require attenuation $\propto r^{-2}$ or steeper to preserve the observed cold gas temperatures of dense cores. This work, however, did not consider attenuation by the accretion flow near the star, which may produce significant attenuation, and which we investigate here. For our fiducial model we adopt $a = 2$ between the inner and outer disk radii, but we also consider the case where $a = 1$.

There are two additional competing effects that modulate the CR flux. First, mirroring, i.e., the reflection of CRs due to the convergence of field lines, can significantly reduce the flux of cosmic rays (Padovani & Galli 2011). This acts to reduce the CR flux impinging on circumstellar disks from external sources (Cleeves et al. 2013a). In contrast, converging field lines can also focus the CR flux via funneling (Padovani & Galli 2011; Silsbee et al. 2018). In the case of CRs accelerated at the stellar surface, the field lines *diverge*, therefore the CR flux effectively undergoes inverse funneling.

To determine the local CR ionization rate, we begin with the initial shock-accelerated spectrum of CRs at the stellar surface and propagate it, including geometric attenuation and energy losses, through three regimes: (I) between the star and the inner edge of the accretion disk, (II) between the radius of the inner disk and the disk surface, and (III) inside the disk (see Figure 1). Figure 2 shows the evolution of the CR spectrum as it evolves with radius and is shaped by each of the different processes we describe below.

In region I, the CR spectrum is attenuated via inverse funneling and undergoes energy losses due to interactions with gas upstream of the shock. To compute the energy losses due to propagation through accreting material, we assume a completely ionized gas and compute the loss function as a combination of Coulomb and pion-production losses (Mannheim & Schlickeiser 1994; Schlickeiser 2002). Figure 2 shows that losses due to the accretion flow significantly reduce the CR

flux, an impact that is particularly acute for lower-energy particles.

In region I, the flux of CRs is also diminished due to inverse funneling. We define the funneling attenuation factor:

$$f_{\text{funnel}} = \frac{B_*}{B_{\text{disk}}}, \quad (6)$$

where B_* is the magnetic field at the stellar surface and B_{disk} is the field at the disk surface (Cleeves et al. 2013a). Young stars have surface magnetic fields of ~ 1 kG, and their field structure can be described as the sum of a series of multipole moments (Romanova & Owocki 2015). Donati et al. (2008) find that the poloidal field of T Tauri star BP Tauri is largely composed of dipole (50%) and octupole (30%) components with a small fraction of higher-order components (10%). The approximately 10% field remaining is in a toroidal component. Therefore, we adopt

$$f_{\text{funnel}} \propto 0.5r^{-3} + 0.3r^{-7} + 0.1r^{-9}. \quad (7)$$

This implies that if CRs are well coupled to the field, the spectrum declines more steeply than the often-assumed r^{-2} free-streaming limit. For our parameters, inverse funneling typically reduces the flux by a factor of ~ 10 – 100 between the star and inner disk.

In region II, we assume that the field attenuates geometrically (e.g., $a = 2$) and undergoes small energy losses due to interactions with neutral material above the disk ($N_{\text{H}} < 10^{20} \text{ cm}^{-2}$). To compute the energy losses due to gas above the disk we adopt the loss function from Padovani et al. (2009), which assumes the gas is cold and mostly molecular, and compute the column density assuming a number density of $n_{\text{H}} = 10^4 \text{ cm}^{-3}$:

$$N_{\text{H,Core}}(r) = \int_{r_A}^r n_{\text{H}} ds. \quad (8)$$

Interactions between the highest-energy CRs and the neutral gas produce new lower-energy CRs, which increase the number of CRs with energies $E \sim 10^2$ – 10^5 eV as shown in Figure 2. We then compute the effective ionization rate at the disk surface by integrating over the spectrum.

Figure 3 shows the surface ionization rates as a function of radius for various models listed in Table 2. At most radii, the ionization rates are well above the Galactic cosmic-ray background ionization rate of $\zeta \sim 10^{-16} \text{ s}^{-1}$ (Indriolo et al. 2007; Indriolo & McCall 2012). All models predict cosmic-ray ionization rates above the ionization rate, $\zeta \leq 10^{-20} \text{ s}^{-1}$, if Galactic CRs are efficiently shielded by the T-Tauriosphere (Cleeves et al. 2013a).

Within the disk (region III) we adopt the expression from Padovani et al. (2018) to estimate the decline in ionization rate with disk column density, N_{H} :

$$\zeta_{\text{CR}} = \zeta_0 \left(\frac{N_{\text{H}}}{10^{18} \text{ cm}^2} \right)^{-0.34}, \quad (9)$$

where ζ_0 is the ionization rate at the surface of the disk. This formulation takes into account the effect of a wider range of secondary and tertiary products. The dominant source of ionization at surface densities greater than 100 g cm^{-2} is electron–positron production as a result of pion production. We note that the details of the attenuation are sensitive to the

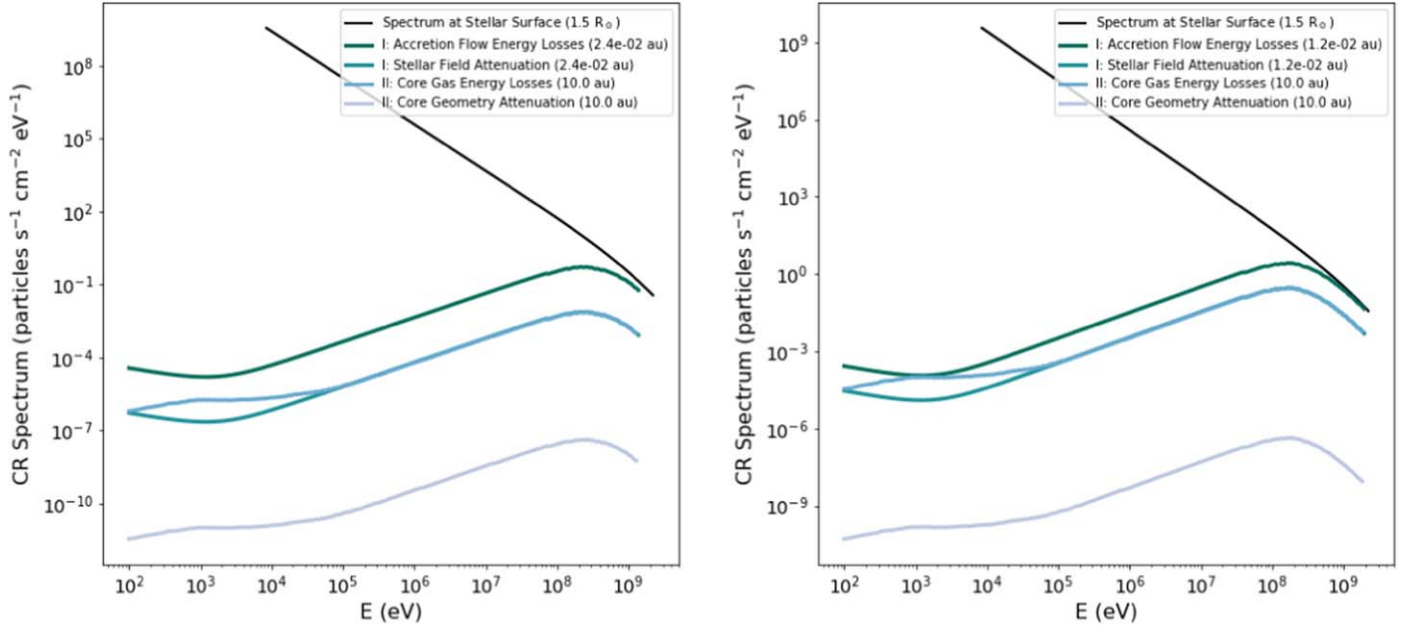


Figure 2. Cosmic-ray spectrum in different regions for the fiducial model (left: $m = 1 M_{\odot}$, $r = 1.5 R_{\odot}$, $\dot{M}_{*} = 10^{-7} M_{\odot} \text{ yr}^{-1}$, and $f_{\text{acc}} = 0.01$) and the high-accretion model (right: $m = 1 M_{\odot}$, $r = 1.5 R_{\odot}$, $\dot{M}_{*} = 10^{-6} M_{\odot} \text{ yr}^{-1}$, and $f_{\text{acc}} = 0.1$).

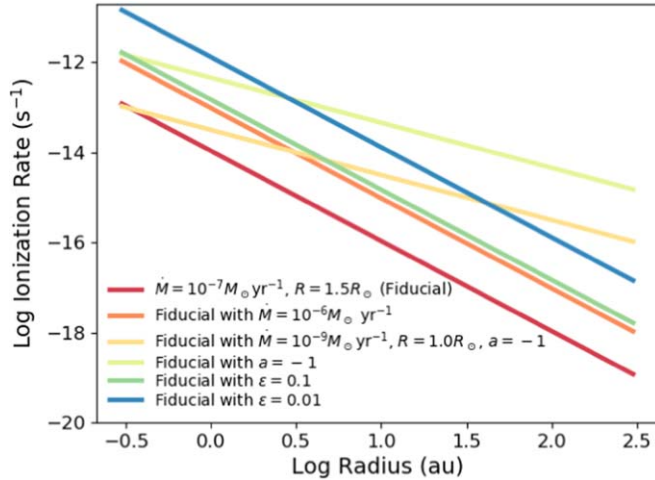


Figure 3. Ionization rate as a function of radius at the disk surface for various model parameters.

spectral shape, the treatment of the interactions, and the inclusion of secondary particles, i.e., additional high-energy particles produced by CR interactions. Padovani et al. (2018) adopt a CR spectrum representing the CR background of the interstellar medium, which follows a different energy dependence than our CR spectrum at the disk surface. However, the results of Padovani et al. (2018) suggest that the ionization rate declines according to a weak power law when $N_{\text{H}} < 10^{25} \text{ cm}^{-2}$ for both “high” and “low” CR spectra, so we assume that the attenuation will be qualitatively similar in our case.

One additional free parameter is the amount of turbulence in the magnetic field. In principle, the CRs and field are well coupled, since the Larmor radius is small: a proton with momentum $3 \text{ GeV}/c$ in a 1 kG field has $r_L < 1.4 \times 10^{-7} R_{\odot}$. The particles would not be expected to scatter more than once per r_L . However, turbulence in the field can change the rate of diffusion (Schlickeiser 2002). Dense cores are expected to be at

least subsonically turbulent, while outflows and disk winds may drive additional turbulence (Offner & Chaban 2017). How this manifests as magnetic turbulence on scales of au, however, is poorly constrained. Rodgers-Lee et al. (2017) define a turbulent diffusion parameter, D , to explore variation in CR propagation, which they vary in the range $3\text{--}380 r_L$. They show that the attenuation of the CR spectrum varies between $\propto r^{-2}$ (free-streaming) ($D = 3 r_L$) and $\propto r^{-1}$ ($D = 380 r_L$) depending on the assumed turbulence and number of scatterings. For the purposes of our fiducial parameters we adopt the attenuation factors as described above and define a coupling parameter, ϵ , which we explore in Section 3.5.

2.4.2. Far-ultraviolet Radiation

FUV radiation from the central star is significant at the disk surface, but it rapidly attenuates with increasing column density. Its contribution becomes negligible by $\Sigma \sim 0.01 \text{ g cm}^{-2}$ (e.g., Perez-Becker & Chiang 2011). Thus, ionization due to FUV irradiation is confined to the disk surface layers.

We adopt a fiducial value for the FUV luminosity of $L_{\text{FUV}} = 10^{30} \text{ erg s}^{-1}$. We then compute the local radiation field as a function of radius:

$$G_0 = \frac{L_{\text{FUV}}}{4\pi r^2} \left(\frac{1}{1.6 \times 10^{-3} \text{ erg s}^{-1} \text{ cm}^{-2}} \right) \quad (10)$$

$$= 1.4 \times 10^4 \left(\frac{L_{\text{FUV}}}{10^{30} \text{ erg s}^{-1}} \right) \left(\frac{r}{3 \text{ au}} \right)^2 \text{ Habing.} \quad (11)$$

The ionization rate due to FUV photons is then

$$\zeta_{\text{FUV}} = G_0 a_X \exp(-b_X A_v) \text{ s}^{-1}, \quad (12)$$

where G_0 is the intensity of the radiation field in Habing units normalized to the typical stellar radiation field, a_X and b_X are the ionization rate coefficients for species X , and A_v is the dust extinction. For atomic carbon, $a_C = 2.1 \times 10^{-10} \text{ s}^{-1}$ and

$b_C = 2.6$ (e.g., McElroy et al. 2013). The reactions associated with FUV are included in the UMIST database.

2.4.3. X-Ray Radiation

X-ray photons have a significantly longer mean free path than FUV photons and serve as an important source of ionization at intermediate column densities (Igea & Glassgold 1999; Glassgold et al. 2007). The X-ray ionization rate can be expressed as a function of the column density of hydrogen nuclei above, N_{Ha} , and below, N_{Hb} , a given location in the disk (Igea & Glassgold 1999; Bai & Goodman 2009):

$$\zeta_X = L_{X,29} \left(\frac{r}{1 \text{ au}} \right)^{-2.2} \times (\zeta_1 [e^{-(N_{\text{Ha}}/N_a)^{\alpha_1}} + e^{-(N_{\text{Hb}}/N_b)^{\alpha_1}}] + \zeta_2 [e^{-(N_{\text{Ha}}/N_a)^{\alpha_2}} + e^{-(N_{\text{Hb}}/N_b)^{\alpha_2}}]), \quad (13)$$

where $L_{X,29} \equiv L_X/10^{29} \text{ erg s}^{-1}$, L_X is the X-ray luminosity, $\zeta_1 = 6 \times 10^{-12} \text{ s}^{-1}$, $\zeta_2 = 10^{-15} \text{ s}^{-1}$, $\alpha_1 = 0.4$, $\alpha_2 = 0.65$, $N_a = 1.5 \times 10^{21} \text{ cm}^{-2}$ and $N_b = 7 \times 10^{23} \text{ cm}^{-2}$. Here, we consider only one surface of the disk, adopt an X-ray energy of $T_x = 3 \text{ keV}$, and assume that the X-ray flux from below is negligible, which is a good approximation as we will show in Section 2.4. The X-ray luminosity correlates with stellar mass, although there is large scatter and a dependence on the stellar evolution model assumed (Feigelson et al. 2005; Preibisch et al. 2005). For the fiducial model we adopt $L_X = 5 \times 10^{29} \text{ erg s}^{-1}$ (e.g., Bai & Goodman 2009). This is comparable to the X-ray luminosity expected for a 0.3–1 M_\odot star according to the relation found by Preibisch et al. (2005):

$$\log_{10}(L_X[\text{erg s}^{-1}]) = 30.37 + 1.44 \times \log_{10}(M/M_\odot), \quad (14)$$

which was derived empirically from T Tauri sources in the Orion Nebula Cluster. The stellar masses are derived assuming the pre-main-sequence tracks from Siess et al. (2000). Young, active stars that are not accreting also emit X-rays, interestingly, at a rate that is ~ 2 times higher than their non-accreting counterparts. We expect this difference occurs because, like cosmic rays, X-rays are attenuated by the accretion flow. We consider a model with $L_X = 10^{29} \text{ erg s}^{-1}$ for comparison.

2.4.4. Radionuclides

In the disk midplane, which is well shielded from all other ionizing sources, the decay of short-lived radionuclides such as ^{26}Al , ^{60}Fe , and ^{36}Cl provides ionization (Cleeves et al. 2013b). Cleeves et al. (2013b) find that the associated ionization rate depends weakly on time and surface density:

$$\zeta_{\text{RN}} = 2.5 \times 10^{-19} \left(\frac{1}{2} \right)^{1.04t} \left(\frac{\Sigma}{1 \text{ g cm}^{-2}} \right)^{0.27} \text{ s}^{-1}. \quad (15)$$

For our UCLCHEM calculations, we adopt a constant value of $\zeta = 2.3 \times 10^{-19} \text{ s}^{-1}$, equivalent to $t = 1 \text{ Myr}$ and $\Sigma = 10 \text{ g cm}^{-2}$, throughout the disk. This effectively places a floor on the ionization rate. Ionization produced by short-lived radionuclides dominates only in regions at large radii and close to the midplane, where other sources of ionization are absent. Long-lived radionuclides also provide ionization, but they

contribute at the level of a few 10^{-22} s^{-1} (e.g., Umebayashi & Nakano 2009; Padovani et al. 2018).

3. Results

3.1. Ionization Rate Distribution

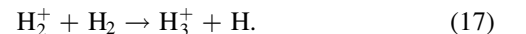
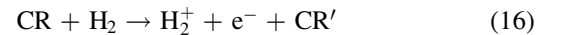
Stellar CR feedback produces significant ionization in the disk. Figure 4 shows the ionization rate computed using the relations in Section 2.4 as a function of the disk surface density. The dominant source of ionization is indicated by shading. While non-accreting sources are expected to produce ionization close to the star and throughout a layer at the disk surface, CRs accelerated by accretion shocks extend the degree of ionization near the midplane. For our fiducial model (top), the ionization rate exceeds 10^{-17} s^{-1} for $r \lesssim 10 \text{ au}$ while $\Sigma > 10 \text{ g cm}^{-2}$. While non-accreting sources may also accelerate CRs (e.g., Rodgers-Lee et al. 2017), these have a minor effect on the disk ionization, primarily dominating the ionization within a few au. The figure shows that in the absence of locally accelerated CRs, ionization produced by short-lived radionuclides dominates at high column densities.

The region with high ionizing flux grows with increasing accretion rate. Figure 4 shows a comparison between the fiducial and high accretion models, for which the accretion rates differ by a factor of 10. Higher accretion extends the radius at which CR ionization dominates by a factor of 3. Although the cosmic-ray flux at the star scales proportionally with the accretion rate, this factor of 10 gain is somewhat offset by the denser accretion flow, which causes additional attenuation. For our fiducial accreting T Tauri stars, ionization caused by CRs is negligible only when $\dot{M}_* < 10^{-9} M_\odot \text{ yr}^{-1}$ and the shock becomes too weak.

These results suggest that young, accreting sources may experience higher ionization in their inner disks than older, non-accreting sources. This has implications for disk chemistry and angular momentum transport in protoplanetary disks as we discuss below.

3.2. Disk Ionization and Chemistry

The local ionization rate is a crucial factor in disk chemistry (van Dishoeck 2014). Thus, enhanced ionization due to CRs may significantly impact the abundance of ionized species, the fraction of free electrons, and the properties of ices. Figure 5 shows the ion fraction, the fractional abundance of positive ions, annotated by the dominant ion species throughout the disk. At the disk surface the ionizing flux due to FUV photons dominates and the gas layer is essentially a photodissociation region (PDR), where atomic ions such as C^+ , S^+ , H^+ , and Mg^+ are the most abundant. At progressively higher column densities the more abundant atomic ions, such as carbon, become neutral. The edge of the PDR occurs around $\Sigma \sim 10^{-2} \text{ g cm}^{-2}$; thereafter H_3^+ is the most abundant ion. H_3^+ is a well-known product of reactions caused by the CR ionization of H_2 (Dalgarno 2006):



Consequently, the H_3^+ abundance is often used as a direct measure of the CR ionization rate (Indriolo & McCall 2012; Gaches et al. 2019a). However, H_3^+ may also be produced by

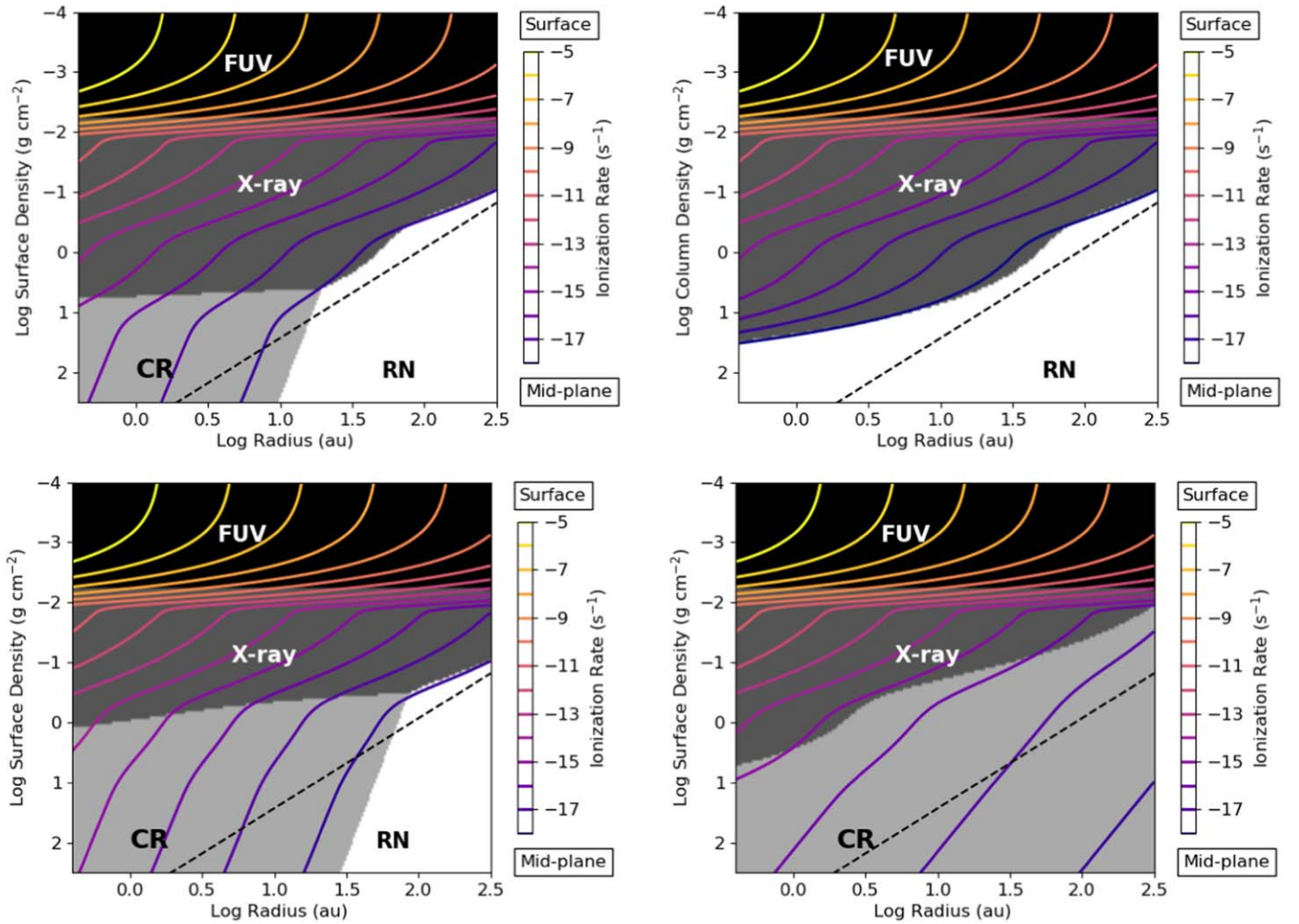
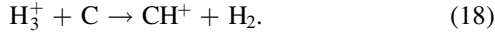


Figure 4. Ionization rates as a function of surface density and radius. Shading indicates the dominant source of ionization due to FUV radiation (black), X-ray radiation (dark gray), cosmic rays (CR, light gray), and short-lived radionuclides (RN, white). Top left: fiducial model for a $1 M_{\odot}$ T Tauri star accreting at a rate of $10^{-7} M_{\odot} \text{ yr}^{-1}$ (see Table 2). Top right: fiducial model but without CRs. Bottom left: high accretion model ($\dot{M}_{*} = 10^{-6} M_{\odot} \text{ yr}^{-1}$). Bottom right: model with diffusive CR attenuation in region II ($\zeta \propto r^{-1}$).

X-ray ionization (Gredel et al. 2001). In our treatment, both X-rays and CRs result in H_3^{+} production.

A variety of additional ion-neutral reactions follow from the presence of H_3^{+} ions, and this species serves as a gateway to more complex chemistry (Tielens 2005; Dalgarno 2006). Notably, C_3H_5^{+} makes a brief appearance as the most abundant ion in the simple network run at early times with small dust grains. This occurs because H_3^{+} also initiates the formation of hydrocarbon radicals (Tielens 2005):



The reaction of CH^{+} with molecular hydrogen then forms hydrocarbon ions such as CH_3^{+} and CH_5^{+} . Together with C^{+} , hydrocarbon reactions produce increasing molecular complexity.

Like Perez-Becker & Chiang (2011), we find that ionized carbon and sulfur are abundant in the disk surface layers due to the stellar FUV field. However, when heavier elements are included in our network, magnesium replaces sulfur as the dominant ion at $\Sigma \sim 10^{-2} \text{ g cm}^{-2}$ and the ion fraction increases by a factor of a few. Reactions with magnesium and nitrogen supplant the formation of complex hydrocarbon radicals close to the disk surface. In general, ionization

produced by X-rays and CRs shifts the ion/neutral transition region to slightly lower column densities.

3.3. Time-dependent Chemical Evolution

UCLCHEM solves for the species abundances as a function of time, which provides insight into the chemical evolution. Our calculations assume steady-state density and temperature distributions. This is a reasonable approximation on the timescale of the rotational period of the disk:

$$t_{\text{dyn}} \simeq \frac{2\pi r}{\sqrt{GM_{*}/r}} = 1 \left(\frac{M_{*}}{1 M_{\odot}} \right)^{-1/2} \left(\frac{r}{1 \text{ au}} \right)^{3/2} \text{ yr}. \quad (19)$$

Figure 5 shows the ionization fraction at $\sim 10^3$ yr (left) and 10^5 yr (right). The disk chemistry reaches an equilibrium quickly and the abundances at the two times are remarkably similar. The most significant changes occur near the disk surface at large radii. There is a brief appearance of C_3H_5^{+} in the PDR transition region for small grains; otherwise, the dominant ion species is largely time-independent. Since we assume that initially half of the hydrogen is molecular and half is atomic, these changes represent a maximum chemical evolutionary progression for the

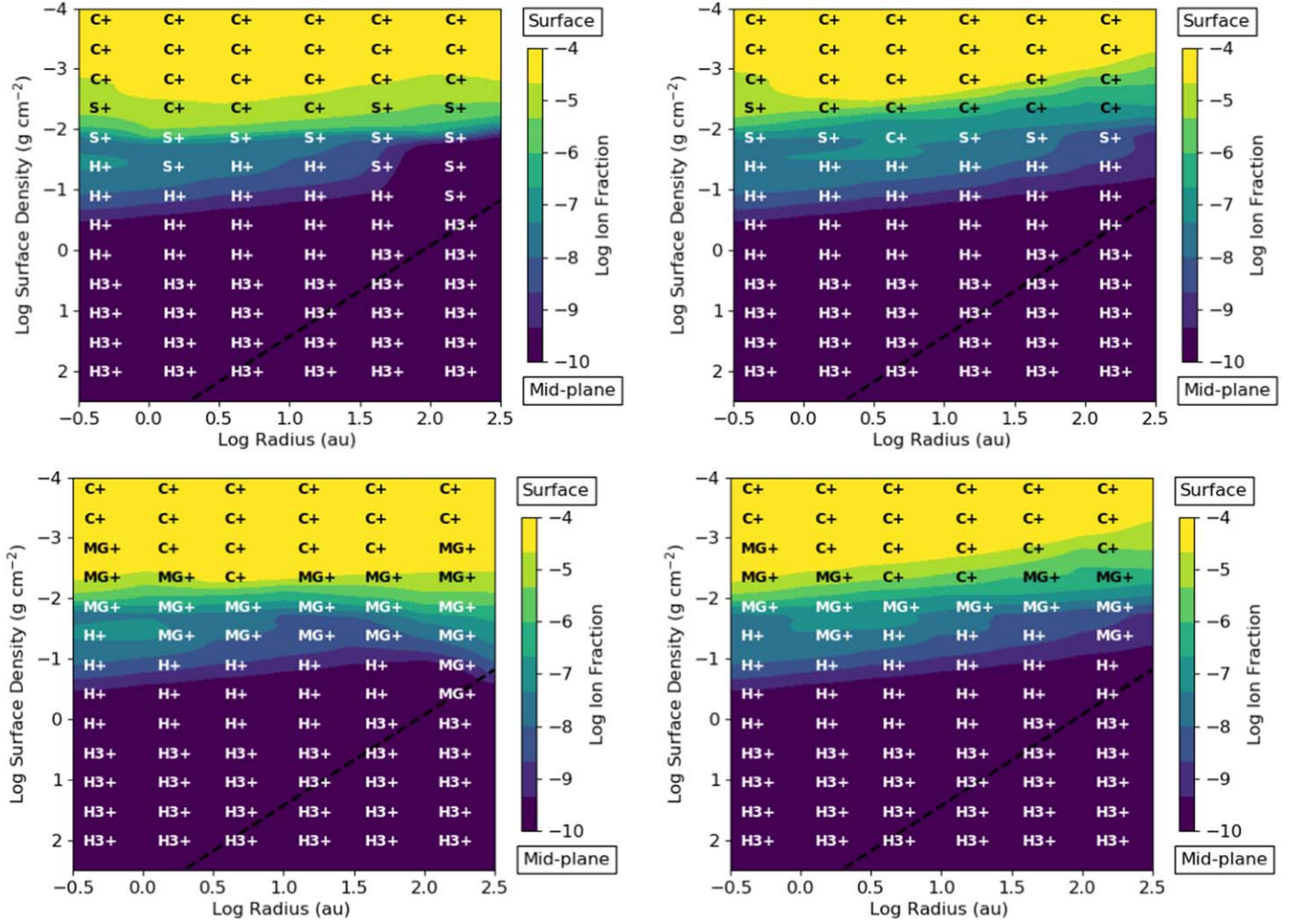


Figure 5. Fraction of positive ions, $n_{\text{ion}}/n_{\text{H}}$, annotated with the most abundant ion. Top: fiducial model computed without metals (only H, He, C, and O) after $t \sim 10^3$ yr of evolution (left) and $\sim 10^5$ yr of evolution (right). Bottom: fiducial model including Mg, N, and Si after $t \sim 10^3$ yr of evolution (left) and $\sim 10^5$ yr of evolution (right).

disk upper layers given time-independent CR and radiative fluxes (see Section 4.1 for further discussion). For the remainder of our figures we show results for $t = 10^3$ yr. Note that the UCLCHEM time step is set by the shortest reaction rates, such that even at this early time the network has advanced hundreds of iterations.

3.4. Activation of the Magnetorotational Instability

3.4.1. Calculation of the MRI-active Region

The MRI requires sufficient ionization in order for the gas to couple with the magnetic field. The instability can be characterized by two dimensionless numbers: the magnetic Reynolds number, Re , quantifies how well the plasma is coupled with the field, while the ambipolar diffusion number, Am , quantifies how well the neutral gas is coupled to the plasma. The magnetic Reynolds number is defined as

$$Re \equiv \frac{c_s h}{\eta} \simeq 1 \left(\frac{x_e}{10^{-13}} \right) \left(\frac{T}{100 \text{ K}} \right)^{1/2} \left(\frac{r}{\text{au}} \right)^{3/2}, \quad (20)$$

where c_s is the local sound speed, $h = c_s/\Omega$ is the scale height, Ω is the Keplerian orbital frequency, and η is the magnetic

diffusivity (e.g., Blaes & Balbus 1994; Perez-Becker & Chiang 2011):

$$\eta = 234 \left(\frac{T}{\text{K}} \right)^{1/2} x_e^{-1} \text{ cm}^2 \text{ s}^{-1}, \quad (21)$$

where $x_e = n_e/n_{\text{H}}$ is the fractional abundance of electrons by number. Am represents a collision timescale between the ions and neutrals:

$$Am \equiv \frac{n_{\text{charge}} \beta_{\text{in}}}{\Omega}, \quad (22)$$

where $n_{\text{charge}} = x_{\text{charge}} n_{\text{tot}}$ is the total number density of singly charged species and $\beta_{\text{in}} \simeq 2 \times 10^{-9} \text{ cm}^3 \text{ s}^{-1}$ is the collisional rate coefficient for singly charged species to distribute their momentum to neutrals.

Numerical simulations suggest that the MRI is active for magnetic Reynolds numbers of 10^2 – 10^4 (Sano & Stone 2002; Turner et al. 2007). Here, we adopt $Re > 3000$, which global disk simulations suggest is the minimum value for fully active MRI (Flock et al. 2012b). Early work by Stone et al. (1998) found that the MRI also requires $Am > 10^2$; however, more recent simulations including ambipolar diffusion by

Bai & Stone (2011) showed that magnetized disks may be MRI-unstable for any value of Am . Cleeves et al. (2013a) note that constraints based on Am also depend on the magnetic field strength and the ratio of thermal to magnetic pressure, β . Following Cleeves et al. (2013a), we define the MRI-active region according to $Re > 3000$ and $Am > 0.1$.

Assuming efficient angular momentum transport via the MRI, the disk mass accretion rate can be written in terms of an α -disk model (e.g., Perez-Becker & Chiang 2011):

$$\dot{M} = 2 \times 3\pi\Sigma\nu = 6\pi\Sigma \times \max \alpha \times \frac{kT}{\mu\Omega}, \quad (23)$$

where the effective viscosity is given by $\nu = \alpha c_s h$ and $\mu = 2.4 \times 10^{-24}$ g is the mean molecular weight. The factor of 2 accounts for accretion along the top and bottom disk surfaces. To compute the value of α , we adopt the relation between α and Am from numerical simulations (Bai & Stone 2011):

$$\max \alpha = \frac{1}{2} \left[\left(\frac{50}{Am^{1.2}} \right)^2 + \left(\frac{8}{Am^{0.3}} + 1 \right)^2 \right]. \quad (24)$$

3.4.2. Cosmic-Ray-mediated MRI

Figures 6 and 7 show the distribution of disk properties for our fiducial model with and without metals. The dashed line in all panels indicates the location of the midplane for a minimum-mass solar nebular (MMSN) disk. The region above this line is representative of older T Tauri-type stars, while more massive, circumstellar disks around younger stars would include gas below this line.

The electron fraction (top left panel) decreases smoothly with disk surface density following the declining ionization rate (see also Figure 4). The number density of positive ions, n_{ion} (top right panel), depends both on the local density, which increases toward the midplane, and on the local ionization rate. The band in the top third of the plot coincides with the high-ionization FUV-dominated region. A band also appears in the bottom third of the disk. This occurs where the ion number density reaches the minimum value set by the combined ionization from radionuclides and CRs. The hashed region indicates where CR ionization dominates over ionization produced by X-ray and FUV photons.

The middle panels in Figures 6 and 7 show the magnetic Reynolds number and ambipolar diffusion number. As described above, we adopt $Re > 3000$ and $Am > 0.1$ to determine the MRI-active region. For the fiducial models, approximately the top half of the parameter space satisfies the magnetic Reynolds criterion, while nearly all satisfies the ambipolar diffusion criterion.

Altogether, we find that the disk surface layers are MRI-active (bottom right panel), and the disk is MRI-active for $\Sigma \sim 1$ g cm $^{-2}$ inside ~ 20 au. The MRI-active region exhibits accretion rates of $\dot{M}_* \lesssim 10^{-7} M_\odot \text{ yr}^{-1}$ (bottom left panel). This is consistent with the accretion rate of $10^{-7} M_\odot \text{ yr}^{-1}$ we adopt for the fiducial model. Although the alpha viscosity in the MRI-active region is reasonably high, $\alpha = 10^{-3}$ – 10^{-1} , suggesting that accretion proceeds efficiently, the low gas density in this region conspires to produce low net accretion. If MRI can occur for $10^2 < Re < 3000$, the MRI-active region would extend down to a few 10 g cm $^{-2}$. Meanwhile, in all scenarios, the disk midplane, $\Sigma \lesssim 10^2$ g cm $^{-2}$, is a dead zone.

We find that the addition of N, Mg, Cl, and Si to the chemical network has a minor impact on the disk properties. The magnetic Reynolds number and alpha viscosity increase slightly throughout the disk, but the boundaries of the MRI-active region remain similar.

The dust grain size has a significant effect on the MRI, which has previously been noted in prior work (Sano et al. 2000; Wardle 2007; Glassgold et al. 2017). This result remains true in the presence of high CR fluxes. The left panel of Figure 8 shows the MRI-active region for the fiducial model and the models with small ($a_{\text{gr}} = 0.1 \mu\text{m}$) and large ($a_{\text{gr}} = 10 \mu\text{m}$) dust grains. By efficiently binding electrons, small grains reduce the MRI-active region by an order of magnitude. For large grains the active region reaches surface densities of $\Sigma \sim 10$ g cm $^{-2}$ and most of the outer disk becomes MRI-active.

We plot the boundary of the MRI-active region for a variety of models, including those shown in Figures 6 and 7, in Figure 8. We discuss the impact of other parameters on the MRI-active region below.

3.5. Cosmic-Ray Attenuation and Magnetic Turbulence

The coupling between the mean magnetic field and the CRs is mediated by the degree of turbulence (Rodgers-Lee et al. 2017; Bai et al. 2019; Thomas & Pfrommer 2019). Within dense cores, the level of turbulence depends on a variety of complex variables including the mean magnetic field and initial conditions inherited from the environment, infall from the gas envelope, and local turbulent driving by the protostellar outflow and disk wind (Offner & Chaban 2017). CRs, by themselves, may also excite magnetic waves, thereby driving turbulence (Schlickeiser et al. 2016). Consequently, the number of scatterings and how the CRs diffuse change significantly (Rodgers-Lee et al. 2017). To investigate this uncertainty, we vary the radial attenuation between the free-streaming and diffusive limits. In the fiducial models we assume that CRs free-stream once they leave the accretion flow (i.e., $a = 2$). Figure 8 shows the change in the MRI-active region if $a = 1$ for the fiducial and low-accretion models. In these models, the CR ionization rate exceeds 10^{-14} s $^{-1}$ at the disk surface for $r \lesssim 30$ au. This higher ionization extends the MRI-active region to surface densities of a few g cm $^{-2}$ for these radii. This suggests that only extreme cosmic-ray fluxes can trigger the MRI in regions near the midplane for radii greater than ~ 30 au.

The fiducial model also assumes that the CRs are well coupled to the gas until they reach the disk inner edge. This means that the CRs must travel upstream through the accretion flow and thus attenuate significantly before reaching the disk. If the accretion flow is turbulent or if it is variable, such that the column density of gas along the CR path is reduced, the CRs will experience less attenuation. We introduce a parameter ϵ to quantify the interaction between the CRs and the accretion flow. A value of $\epsilon = 1$ indicates the accretion rate is constant and the CRs traverse the full accretion column, i.e., they are perfectly coupled to the magnetic field in the accretion column and thus suffer energy losses due to their interactions with the gas as they travel between the star and the disk. Lower values of ϵ represent imperfect coupling with the magnetic field and/or a decline in the upstream accretion rate by a factor of ϵ , two factors that reduce the magnitude of the CR energy losses. If the CRs are able to diffuse out of the high-density accretion

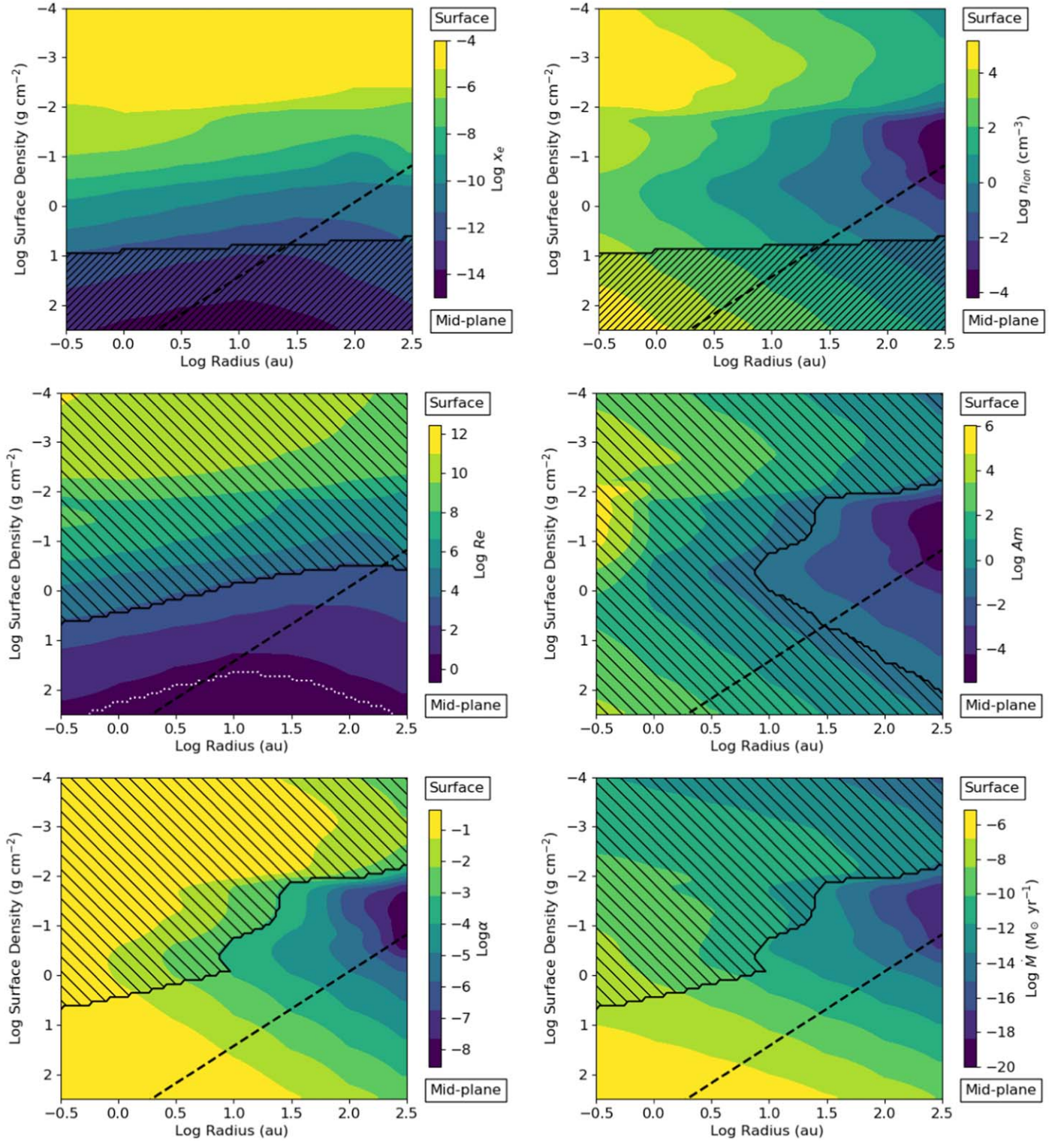


Figure 6. Electron fraction, ion number density, magnetic Reynolds number, ambipolar diffusion number, viscosity parameter, and accretion rate for our fiducial model ($1 M_{\odot}$ T Tauri star with accretion rate of $\dot{M}_{*} = 10^{-7} M_{\odot} \text{ yr}^{-1}$). The dashed line indicates the surface density at the midplane of an MMSN disk. In the top plots, the hashed region indicates where the CR ionization dominates over FUV and X-rays. In the middle plots, the hashed region represents $Re > 3000$ (left) and $Am > 0.1$ (right), while the white dotted line indicates where $Re = 10^2$. In the bottom plots, the hashed region indicates where the MRI is active (i.e., $Re > 3000$ and $Am > 0.1$).

column, then they will propagate through significantly less material. So $\epsilon = 0.1$ represents a scenario in which CRs on average traverse only 10% of the gas in the accretion column. Alternatively, the CRs may interact with a smaller column of gas if accretion has declined by the time they escape from the

accretion shock, and the gas density in the accretion column is lower. Thus, $\epsilon = 0.1$ may also represent the case when the accretion has declined by a factor of 10, but the CRs remain coupled to the magnetic field. Consequently, ϵ provides a crude way of parameterizing some of our uncertainty about the

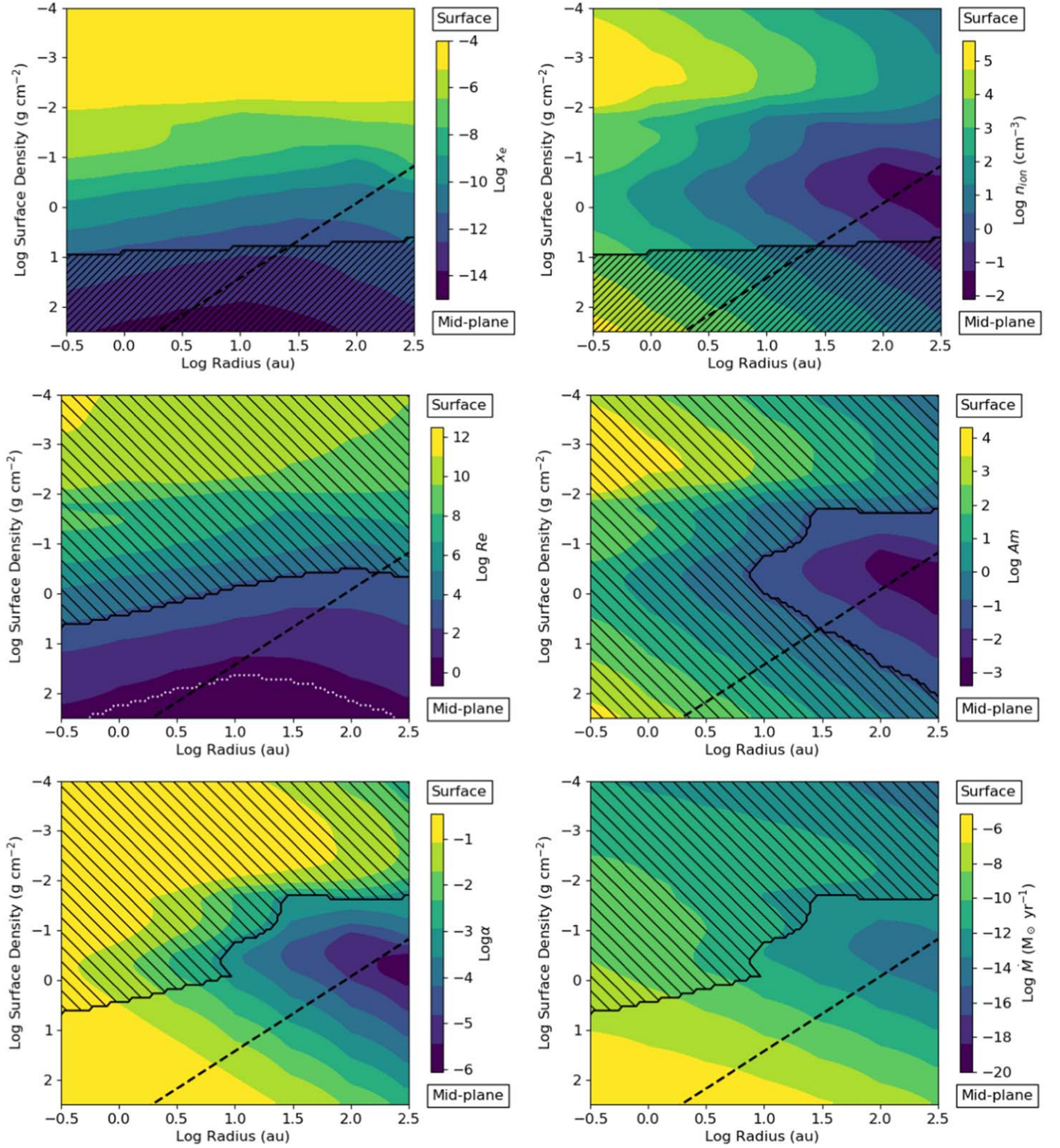


Figure 7. Same as Figure 6 but for the fiducial model with the full network.

energy losses experienced by the CRs between the star and the disk.

The right panel of Figure 8 shows the MRI-active region for $\epsilon = 0.1$ and $\epsilon = 0.01$. Figure 8 shows that reducing the attenuation caused by accreting gas increases the MRI-active region to higher surface densities as expected. However, the midplane of the disk remains MRI-inactive.

4. Discussion

4.1. Implications for Disk Evolution: Accretion Variability

The luminosity of young stellar objects is known to be variable on timescales ranging from hours to hundreds or possibly thousands of years (Audard et al. 2014). The magnitude of the change in luminosity appears to correlate

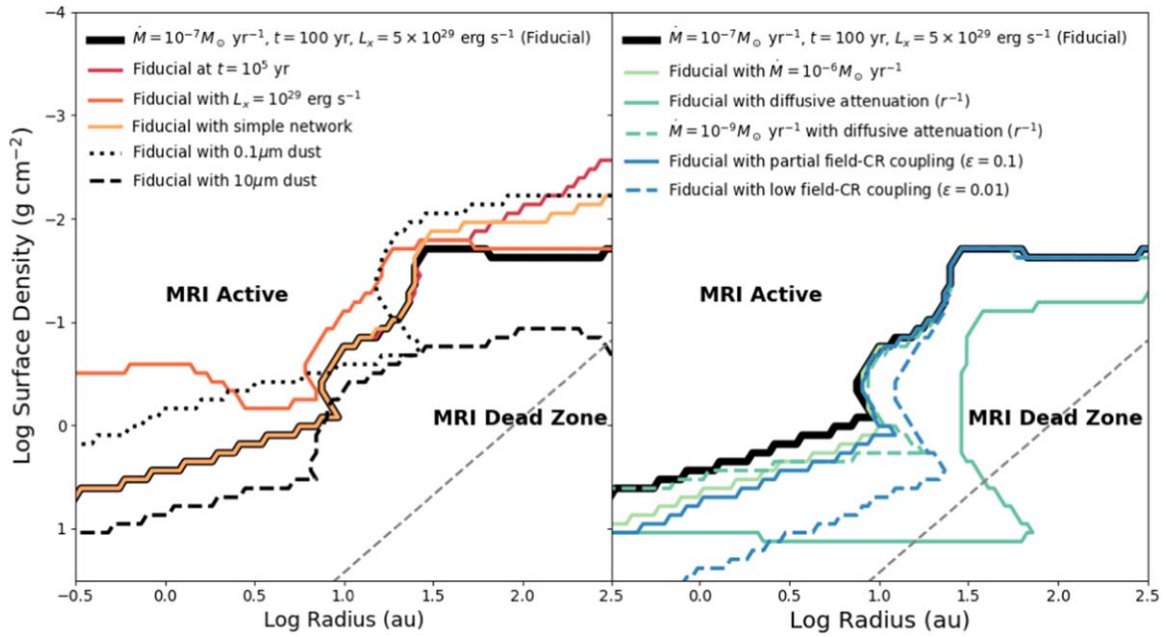


Figure 8. Boundary between the MRI-active ($Re > 3000$, $Am > 0.1$) and MRI-dead zones for the fiducial model (thick black line) and variations.

with frequency in that changes of order unity are common, while changes by orders of magnitude, like FU Ori-type bursts, are rare (Offner & McKee 2011; Hillenbrand & Findeisen 2015). Short-term changes in luminosity lasting months to a few years are generally attributed to inner disk variation, which could be caused by changes in disk morphology or the accretion flow (e.g., Rebull et al. 2014).

Our results show that CRs accelerated by accretion shocks impact disk chemistry and thereby mediate stellar accretion. Consequently, CR feedback provides a mechanism to self-regulate accretion as follows. If the accretion rate declines, stellar CRs are less attenuated by the accretion flow, and the CR flux reaching the disk increases. This causes the MRI-active region to expand, thereby increasing the disk accretion rate. Once the accretion rate increases, the CR flux reaching the disk declines, reducing the MRI-active region and so on. We expect CR-related variations in accretion to occur on timescales of a few years, as dictated by the disk dynamical time at the edge of the MRI-active region (e.g., Figure 8). However, the magnitude of variation depends on the details of the CR propagation.

Our models predict that CRs will be efficiently accelerated down to accretion rates of $\sim 10^{-9} M_{\odot} \text{ yr}^{-1}$. Thus, CR feedback is likely important for most T Tauri stars. Higher accretion rates produce higher CR fluxes, but the attenuation of the dense accretion flow is also more severe. This suggests that CRs accelerated in protostellar accretion shocks may not influence the chemistry of their disks as strongly. However, protostellar outflow may advect some of these CRs outward (e.g., Rodgers-Lee et al. 2017) and thereby allow them to influence the chemistry of the natal core and molecular cloud.

Constraining the variability in luminosity of deeply embedded protostellar sources is challenging, since it is difficult to directly observe bursts. However, observations of molecules in the gas phase, such as CO, which quickly freeze out at high densities and low temperatures, are thought to provide evidence of past accretion bursts (e.g., Jørgensen et al. 2015; Frimann et al. 2016). Although there are a number of

uncertainties, this line of inquiry suggests that variability in accretion by a factor of a few to 10 is relatively common in young objects on thousand-year timescales. The origin of this variability is debated, and it is often attributed to perturbations by a companion or gravitational disk instability rather than MRI variation (Audard et al. 2014). However, independent of origin, the byproduct of the enhanced accretion, CRs, are likely to also impact the observed abundances. In general, we expect CRs to enhance the gas-phase CO and thus reduce the luminosity needed to produce the observed CO emission (e.g., Gaches et al. 2019b). Thus, CRs accelerated via accretion shocks have implications not only for modulating disk variability but also for constraining the true frequency of accretion bursts and their underlying physical origin.

4.2. Implications for Complex Disk Chemistry

The additional ionization provided by local CRs also has implications for the formation and abundance of complex organics. For example, ionization is important to the gas-phase production of methyl cyanide (CH_3CN), since its main gas-phase formation pathway requires CH_3^+ ($\text{HCN} + \text{CH}_3^+$) (Walsh et al. 2014; Öberg et al. 2015). Ionization rates of 10^{-14} s^{-1} could explain the large ratio of CH_3CN to HCN observed in the MWC 480 protoplanetary disk (Öberg et al. 2015). We find that the ratio $\text{CH}_3\text{CN}/\text{HCN} > 0.1$ and large CH_3CN abundance are reproduced in our model through gas-phase chemistry driven by ionization for $\Sigma < 10^{-2} \text{ g cm}^{-2}$ at 100 au. However, disk turbulence that produces vertical mixing may still be important if CH_3CN is abundant outside of the region in which it is produced, as predicted by Öberg et al. (2015).

4.3. Implications for Disk Turbulence

Despite the enhanced ionization rates at the disk surface, our models predict that the MRI is weak or absent at the disk midplane. This is consistent with recent observations of protoplanetary disks using the linewidth of CO isotopologues to place constraints on disk turbulence. The level of turbulence

observed in protoplanetary disks is quite low, and recent observations place upper limits of $v_{\text{turb}} \lesssim 0.08c_s$ on the turbulence in the outer disk ($r \gtrsim 50$ au) near the midplane (Flaherty et al. 2015, 2017, 2018). Even with the Atacama Large Millimeter/submillimeter Array, resolved observations of protoplanetary disks are challenging, however, and there are many uncertainties, e.g., Teague et al. (2016) report $v_{\text{turb}} = 0.2\text{--}0.4c_s$ for TW Hya.

4.4. Comparison with Past Work

Our results are consistent with Bai & Goodman (2009), who adopt a simpler network but include heating and cooling. For the same X-ray luminosity, $L_X = 5 \times 10^{29} \text{ erg s}^{-1}$, but no CR ionization they predicted an MRI-active region down to $\Sigma = 30\text{--}50 \text{ g cm}^{-2}$, including the MMSN disk midplane beyond 50 au, given an MRI-active threshold of $Re > 100$. Bai & Goodman (2009) showed that including a constant CR ionization rate of $\zeta = 10^{-17} \text{ s}^{-1}$ further extends the MRI-active region. We find a similar result for the same threshold of magnetic Reynolds number modulo our higher local CR ionization rate (see dotted line in our Figures 6 and 7). More recent numerical work has since revised the threshold of magnetic Reynolds number for active MRI (Flock et al. 2012a), which directly leads to the conclusion that the midplane is an MRI-dead zone.

Our models produce a similar ionization rate distribution to Cleeves et al. (2013a) given similar X-ray, FUV, radionuclide, and CR parameters. However, we find electron abundances that are lower by a factor of 10–100 near the midplane. This difference leads Cleeves et al. (2013a) to conclude that under similar conditions most of the disk is MRI-active (e.g., their Figure 14), while we conclude that the midplane is generally inactive. They adopt a more accurate treatment of X-ray ionization, including a hard X-ray spectrum, but the discrepancies in our results may also be due to differences between our chemical networks. The network adopted by Cleeves et al. (2013a) is simpler and includes fewer grain reactions. Recent observations suggest minimal MRI activity at large radii near the disk midplane, which we find here (see Section 4.3).

4.5. Impact of the Hall Effect on Disk Stability

In our analysis we assume that the diffusivity is dictated by ohmic dissipation, a regime in which both ions and electrons are decoupled from the magnetic field, following the convention of a number of past studies (e.g., Stone et al. 1998; Bai & Goodman 2009; Perez-Becker & Chiang 2011; Cleeves et al. 2013a). However, electrons and ions tend to be well coupled to the field at lower density. Ambipolar diffusion occurs when both ions and electrons are coupled to the field. This effect dominates at low column densities, when the gas is well ionized, specifically at the disk surface and in the outer disk. Hall diffusion, in which only electrons are coupled to the field, is important at intermediate densities, while ohmic diffusion only dominates at high densities (Wardle 2007). In this work we are mainly concerned with the impact of CRs on the MRI-active region at intermediate to high densities, and thus the distinction between the ohmic and Hall diffusion-dominated regions is potentially important. The Hall effect has the peculiar feature of depending on both the magnitude and direction of the magnetic field. Wardle & Salmeron (2012) compare the relative importance of Hall and ohmic diffusion to the MRI and

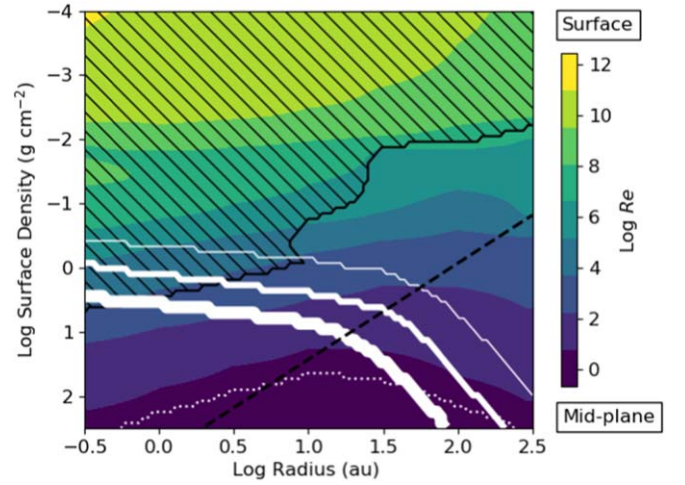


Figure 9. Magnetic Reynolds number for the fiducial model with the corresponding MRI-active region overlaid. The white solid lines indicate the MRI limit in the case of anti-aligned rotation and magnetic field vectors for $B_z = 1$ G (thick), $B_z = 0.1$ G (intermediate), and $B_z = 0.01$ G (thin) as defined by Equation (25).

demonstrate that Hall diffusion can increase or decrease the size of the MRI-active region by an order of magnitude depending on the field orientation with respect to the rotation axis of the disk. Reproducing their analysis here is beyond the scope of this work; however, we can assess the limit in the Hall-dominated diffusion regime for $B_z < 0$ (magnetic field anti-aligned with the rotation axis) in which the Hall effect acts to stabilize the disk to the MRI. In this regime, Wardle & Salmeron (2012) derive a criterion for stability based only on the magnetic field strength and the fractional ionization (Wardle & Salmeron 2012):

$$x_e \lesssim \frac{1}{2} \frac{1.4 m_H c \Omega}{e B} \simeq \frac{1.5 \times 10^{-11} (M/M_\odot)^{1/2}}{B/G (r/\text{au})^{3/2}}. \quad (25)$$

Figure 9 shows the MRI boundary for our fiducial model with the limit imposed by the Hall effect from Equation (25) for three different field strengths. We overlay this on the magnetic Reynolds number, which is defined assuming ohmic dissipation in our calculations. This figure shows that the MRI will be suppressed below the critical column density our models predict, but only in the inner disk (\lesssim a few au) and only for weak fields. In contrast, for fields aligned with the disk rotation axis, $B_z > 0$, Wardle & Salmeron (2012) show that the Hall effect enhances the MRI. The Hall effect has also been studied directly in a small number of magnetohydrodynamic simulations. There the Hall-shear instability is found in the $B \cdot \Omega > 0$ case (Kunz 2008) and is observed to produce a substantial amount of radial transport of angular momentum even in the “dead zone” (Bai 2014; Lesur et al. 2014; Simon et al. 2015; Bai & Stone 2017). Thus, in this limit we expect consideration of the Hall effect to increase the size of the MRI-active region beyond that predicted by our models. However, the nature of the field configuration in accretion and protoplanetary disks remains poorly constrained both observationally and theoretically. Additional constraints on the true magnetic field strength and orientation in disks are required to make stronger claims about the influence of the Hall effect on the MRI.

4.6. Caveats

We assume that photons and CRs enter the disk vertically through its top surface and ignore contributions from photons and CRs that enter the disk “sideways” at the inner radius. Consequently, our results underestimate the ionization at the midplane in the inner ~ 10 au due to both X-rays and CRs (Igea & Glassgold 1999; Rodgers-Lee et al. 2017). This additional ionization would likely extend the MRI-active region throughout most of the vertical extent within a few au of the source. In addition, high temperatures, which exceed ~ 800 K in the very inner disk, will thermally ionize alkali atoms, yielding an ionization fraction of up to 10^{-8} s^{-1} (e.g., Fromang et al. 2002; Desch & Turner 2015).

While we account for all the main sources of ionization, our estimation of the MRI is relatively simplistic. We do not directly model the fluid dynamics of the disk (e.g., Simon et al. 2018). Thus, we may miss other dynamical effects. For example, Gole & Simon (2018) find that the FUV-irradiated surface layers may affect the magnetic structure of the disk by transporting magnetic flux to the midplane, thereby suppressing the MRI.

We do not self-consistently model grain growth, which is especially important at the disk midplane, where grains coagulate and sediment (Dullemond & Dominik 2004). A vertically variable dust distribution may modify the details of our results somewhat.

We also do not explicitly follow charged grains. Charged grains may impact our MRI analysis via the ambipolar diffusion number, where the number density of charged species, n_{charge} , can be written including positively and negatively charged grains, i.e., $n_{\text{charge}} = n_{\text{ion}} + n_{Q+} + n_{Q-}$ (e.g., Perez-Becker & Chiang 2011). To roughly constrain the impact of charged grains on our results we use the abundance of electrons sticking to dust grains to compute the average charge per grain. We find that grains near the disk surface ($\Sigma \lesssim 0.1 \text{ g cm}^{-2}$) are on average strongly positively charged. At higher surface densities ($\Sigma > 0.1 \text{ g cm}^{-2}$) grains become slightly negatively charged. Including the number density of charged grains in the calculation of Am has a small effect, since it mainly enhances Am near the disk surface, which is already MRI-active. A more sophisticated grain treatment, including polycyclic aromatic hydrocarbons, is required to quantify the impact of charged grains on the MRI with more accuracy, although the impact of small grains is expected to be modest (Bai 2011; Xu & Bai 2016).

We also make simple assumptions about the geometry of the magnetic field, which has an outsize impact on the propagation of the CRs and local ionization rate, by influencing both the degree of attenuation and the severity of the energy losses (Fraschetti et al. 2018). Some of the stellar CRs may be directed away from the disk by the outflow (Rodgers-Lee et al. 2017), which may cause CR beaming and further reduce the CR flux reaching the disk. Full magnetohydrodynamic simulations, including self-consistent modeling of the stellar, disk, and outflow fields together with cosmic-ray propagation, are required to study the impact of realistic magnetic field configurations (Romanova & Owocki 2015; Bai et al. 2019).

5. Conclusions

In this work, we use the gas-grain astrochemistry code UCLCHEM to investigate the impact of cosmic rays accelerated in accretion shocks on the chemistry of circumstellar disks. We include all major sources of ionization, namely FUV radiation,

X-rays, CRs, and radionuclides, and model the attenuation of each as a function of radius and gas surface density. We explore accretion rates of $\dot{M}_* \sim 10^{-9}$ – $10^{-6} M_{\odot} \text{ yr}^{-1}$ and assess how different treatments of CR propagation and magnetic field–CR coupling influence the ionization rate. We show that locally accelerated cosmic rays can produce ionization rates $\zeta \gtrsim 10^{-14} \text{ s}^{-1}$ at the disk surface within 10 au of the central star. Our results show that local shock-accelerated CRs can produce ionization rates that are several orders of magnitude higher than the rate associated with the Galactic cosmic-ray background.

The cosmic-ray flux from the star enhances the disk ionization at intermediate to high surface densities ($\Sigma > 10 \text{ g cm}^{-2}$), particularly within 10 au of the star. We show that C^+ , S^+ , and Mg^+ are the dominant ions in the disk surface layers, while H_3^+ ions dominate at surface densities above 1.0 g cm^{-2} .

We use the electron fraction and ion number density to predict the radii and surface densities where the MRI is active. We show that ionization by local cosmic rays extends the MRI-active region toward the disk midplane. However, the midplane of a minimum-mass solar nebula disk remains an MRI-dead zone unless cosmic rays propagate outward through diffusion ($\zeta \propto r^{-1}$).



We note an important feedback loop circumscribed by the relationship between the cosmic-ray flux, which scales with the accretion rate, the column density of the accretion flow, which attenuates cosmic rays, and the MRI, which is enhanced by cosmic-ray ionization and in turn promotes accretion. This relationship limits the efficacy of cosmic-ray ionization in disks at very high accretion rates, i.e., in protostellar disks. In contrast, the disks around T Tauri stars experiencing accretion rates of $\dot{M}_* = 10^{-9}$ – $10^{-7} M_{\odot} \text{ yr}^{-1}$ will be significantly influenced by cosmic rays accelerated by accretion.

In summary, we conclude that cosmic rays are a substantial source of ionization in the disks of young, accreting stars. Future work is required to explore the impact of magnetic field geometry on the cosmic-ray attenuation and the evolution of the spectrum.

S.S.R.O. and B.A.L.G. acknowledge support from the National Science Foundation (NSF) grant AST-1510021. S.S. R.O. was also supported by NSF CAREER grant AST-1650486. The authors thank an anonymous referee for helpful comments that improved the manuscript. The authors also thank Xuening Bai and Marco Padovani for helpful discussions. The authors acknowledge the Texas Advanced Computing Center (TACC) at The University of Texas at Austin for providing HPC resources that have enabled the research reported within this paper.

Software: UCLCHEM (Holdship et al. 2017), MATPLOTLIB (Hunter 2007), NUMPY (van der Walt et al. 2011), SCIPY (Jones et al. 2001), JUPYTERLAB.

ORCID iDs

Stella S. R. Offner  <https://orcid.org/0000-0003-1252-9916>
Brandt A. L. Gaches  <https://orcid.org/0000-0003-4224-6829>

References

- Alexander, R., Pascucci, I., Andrews, S., Armitage, P., & Cieza, L. 2014, in *Protostars and Planets VI*, ed. H. Beuther et al. (Tucson, AZ: Univ. Arizona Press), 475

- Audard, M., Ábrahám, P., Dunham, M. M., et al. 2014, in *Protostars and Planets VI*, ed. H. Beuther et al. (Tucson, AZ: Univ. Arizona Press), 387
- Bai, X.-N. 2011, *ApJ*, 739, 51
- Bai, X.-N. 2014, *ApJ*, 791, 137
- Bai, X.-N., & Goodman, J. 2009, *ApJ*, 701, 737
- Bai, X.-N., Ostriker, E. C., Plotnikov, I., & Stone, J. M. 2019, arXiv:1902.10219
- Bai, X.-N., & Stone, J. M. 2011, *ApJ*, 736, 144
- Bai, X.-N., & Stone, J. M. 2017, *ApJ*, 836, 46
- Balbus, S. A., & Hawley, J. F. 1991, *ApJ*, 376, 214
- Blaes, O. M., & Balbus, S. A. 1994, *ApJ*, 421, 163
- Ceccarelli, C., Dominik, C., López-Sepulcre, A., et al. 2014, *ApJL*, 790, L1
- Cleeves, L. I., Adams, F. C., & Bergin, E. A. 2013a, *ApJ*, 772, 5
- Cleeves, L. I., Adams, F. C., Bergin, E. A., & Visser, R. 2013b, *ApJ*, 777, 28
- D'Alessio, P., Calvet, N., Hartmann, L., Franco-Hernández, R., & Servín, H. 2006, *ApJ*, 638, 314
- Dalgarno, A. 2006, *PNAS*, 103, 12269
- Desch, S. J., & Turner, N. J. 2015, *ApJ*, 811, 156
- Donati, J.-F., Jardine, M. M., Gregory, S. G., et al. 2008, *MNRAS*, 386, 1234
- Dullemond, C. P., & Dominik, C. 2004, *A&A*, 421, 1075
- Dutrey, A., Semenov, D., Chapillon, E., et al. 2014, in *Protostars and Planets VI*, ed. H. Beuther et al. (Tucson, AZ: Univ. Arizona Press), 317
- Favre, C., Ceccarelli, C., López-Sepulcre, A., et al. 2018, *ApJ*, 859, 136
- Feigelson, E. D., Getman, K., Townsley, L., et al. 2005, *ApJS*, 160, 379
- Fiedler, R. A., & Mouschovias, T. C. 1993, *ApJ*, 415, 680
- Flaherty, K. M., Hughes, A. M., Rose, S. C., et al. 2017, *ApJ*, 843, 150
- Flaherty, K. M., Hughes, A. M., Rosenfeld, K. A., et al. 2015, *ApJ*, 813, 99
- Flaherty, K. M., Hughes, A. M., Teague, R., et al. 2018, *ApJ*, 856, 117
- Flock, M., Dzjurkevich, N., Klahr, H., Turner, N., & Henning, T. 2012a, *ApJ*, 744, 144
- Flock, M., Henning, T., & Klahr, H. 2012b, *ApJ*, 761, 95
- Frascchetti, F., Drake, J. J., Cohen, O., & Garraffo, C. 2018, *ApJ*, 853, 112
- Frimann, S., Jørgensen, J. K., Padoan, P., & Haugbølle, T. 2016, *A&A*, 587, A60
- Fromang, S., Terquem, C., & Balbus, S. A. 2002, *MNRAS*, 329, 18
- Gaches, B. A. L., & Offner, S. S. R. 2018, *ApJ*, 861, 87
- Gaches, B. A. L., Offner, S. S. R., & Bisbas, T. G. 2019a, arXiv:1905.02232
- Gaches, B. A. L., Offner, S. S. R., & Bisbas, T. G. 2019b, *ApJ*, 878, 105
- Gammie, C. F. 1996, *ApJ*, 457, 355
- Glassgold, A. E., Lizano, S., & Galli, D. 2017, *MNRAS*, 472, 2447
- Glassgold, A. E., Najita, J. R., & Igea, J. 2007, *ApJ*, 656, 515
- Gole, D. A., & Simon, J. B. 2018, *ApJ*, 869, 84
- Gredel, R., Black, J. H., & Yan, M. 2001, *A&A*, 375, 553
- Gressel, O., Nelson, R. P., & Turner, N. J. 2012, *MNRAS*, 422, 1140
- Hartmann, L., Herczeg, G., & Calvet, N. 2016, *ARA&A*, 54, 135
- Hillenbrand, L. A., & Findeisen, K. P. 2015, *ApJ*, 808, 68
- Holdship, J., Viti, S., Jiménez-Serra, I., Makrymallis, A., & Priestley, F. 2017, *AJ*, 154, 38
- Hunter, J. D. 2007, *CSE*, 9, 90
- Igea, J., & Glassgold, A. E. 1999, *ApJ*, 518, 848
- Indriolo, N., Geballe, T. R., Oka, T., & McCall, B. J. 2007, *ApJ*, 671, 1736
- Indriolo, N., & McCall, B. J. 2012, *ApJ*, 745, 91
- Indriolo, N., Neufeld, D. A., Gerin, M., et al. 2015, *ApJ*, 800, 40
- Johns-Krull, C. M. 2007, *ApJ*, 664, 975
- Jones, E., Oliphant, T., Peterson, P., et al. 2001, *SciPy: Open Source Scientific Tools for Python*, <http://www.scipy.org/>
- Jørgensen, J. K., Visser, R., Williams, J. P., & Bergin, E. A. 2015, *A&A*, 579, A23
- Kunz, M. W. 2008, *MNRAS*, 385, 1494
- Lesur, G., Kunz, M. W., & Fromang, S. 2014, *A&A*, 566, A56
- Manara, C. F., Testi, L., Natta, A., et al. 2014, *A&A*, 568, A18
- Mannheim, K., & Schlickeiser, R. 1994, *A&A*, 286, 983
- McElroy, D., Walsh, C., Markwick, A. J., et al. 2013, *A&A*, 550, A36
- Öberg, K. I., Guzmán, V. V., Furuya, K., et al. 2015, *Natur*, 520, 198
- Offner, S. S. R., & Chaban, J. 2017, *ApJ*, 847, 104
- Offner, S. S. R., Klein, R. I., McKee, C. F., & Krumholz, M. R. 2009, *ApJ*, 703, 131
- Offner, S. S. R., & McKee, C. F. 2011, *ApJ*, 736, 53
- Padovani, M., & Galli, D. 2011, *A&A*, 530, A109
- Padovani, M., Galli, D., & Glassgold, A. E. 2009, *A&A*, 501, 619
- Padovani, M., Ivlev, A. V., Galli, D., & Caselli, P. 2018, *A&A*, 614, A111
- Padovani, M., Marcowith, A., Hennebelle, P., & Ferrière, K. 2016, *A&A*, 590, A8
- Perez-Becker, D., & Chiang, E. 2011, *ApJ*, 735, 8
- Preibisch, T., Kim, Y.-C., Favata, F., et al. 2005, *ApJS*, 160, 401
- Quénard, D., Jiménez-Serra, I., Viti, S., Holdship, J., & Coutens, A. 2018, *MNRAS*, 474, 2796
- Rebull, L. M., Cody, A. M., Covey, K. R., et al. 2014, *AJ*, 148, 92
- Rodgers-Lee, D., Taylor, A. M., Ray, T. P., & Downes, T. P. 2017, *MNRAS*, 472, 26
- Romanova, M. M., & Owocki, S. P. 2015, *SSRv*, 191, 339
- Sano, T., Miyama, S. M., Umebayashi, T., & Nakano, T. 2000, *ApJ*, 543, 486
- Sano, T., & Stone, J. M. 2002, *ApJ*, 577, 534
- Schlickeiser, R. 2002, *Cosmic Ray Astrophysics* (Berlin: Springer)
- Schlickeiser, R., Caglar, M., & Lazarian, A. 2016, *ApJ*, 824, 89
- Semenov, D., Wiebe, D., & Henning, T. 2004, *A&A*, 417, 93
- Siess, L., Dufour, E., & Forestini, M. 2000, *A&A*, 358, 593
- Silsbee, K., Ivlev, A. V., Padovani, M., & Caselli, P. 2018, *ApJ*, 863, 188
- Simon, J. B., Bai, X.-N., Flaherty, K. M., & Hughes, A. M. 2018, *ApJ*, 865, 10
- Simon, J. B., Lesur, G., Kunz, M. W., & Armitage, P. J. 2015, *MNRAS*, 454, 1117
- Stone, J. M., Ostriker, E. C., & Gammie, C. F. 1998, *ApJL*, 508, L99
- Teague, R., Guilloteau, S., Semenov, D., et al. 2016, *A&A*, 592, A49
- Thomas, T., & Pfrommer, C. 2019, *MNRAS*, 485, 2977
- Tielens, A. G. G. M. 2005, *The Physics and Chemistry of the Interstellar Medium* (Cambridge: Cambridge Univ. Press)
- Turner, N. J., Sano, T., & Dziourkevitch, N. 2007, *ApJ*, 659, 729
- Umebayashi, T., & Nakano, T. 1981, *PASJ*, 33, 617
- Umebayashi, T., & Nakano, T. 2009, *ApJ*, 690, 69
- van der Walt, S., Colbert, S. C., & Varoquaux, G. 2011, *CSE*, 13, 22
- van Dishoeck, E. F. 2014, *FaDi*, 168, 9
- Wakelam, V., Cuppen, H. M., & Herbst, E. 2013, arXiv:1309.7792
- Wakelam, V., Herbst, E., Loison, J.-C., et al. 2012, *ApJS*, 199, 21
- Walsh, C., Millar, T. J., Nomura, H., et al. 2014, *A&A*, 563, A33
- Wardle, M. 2007, *Ap&SS*, 311, 35
- Wardle, M., & Salmeron, R. 2012, *MNRAS*, 422, 2737
- Xu, R., & Bai, X.-N. 2016, *ApJ*, 819, 68